Supporting Information

for

Ice crystal sublimation for easily producing MnO_2 cathode with hierarchically porous structure and high cyclic reversibility

Xiangru Si, Ruijie Zhu, Yang Yang, Huijun Yang, Nan Sheng, Chunyu Zhu**

Xiangru Si - School of Low-carbon Energy and Power Engineering, China University of Mining and Technology, Xuzhou 221116, China

Ruijie Zhu - Graduate School of Chemical Sciences and Engineering, Hokkaido University, Sapporo, Hokkaido 060-8628, Japan

Yang Yang - National Institute of Advanced Industrial Science and Technology (AIST), 1-1-1, Umezono, Tsukuba 305-8568 Japan

Huijun Yang - National Institute of Advanced Industrial Science and Technology (AIST), 1-1-1, Umezono, Tsukuba 305-8568 Japan

Nan Sheng- School of Low-carbon Energy and Power Engineering, China University of Mining and Technology, Xuzhou 221116, China

Chunyu Zhu - School of Low-carbon Energy and Power Engineering, China University of Mining and Technology, Xuzhou 221116, China

Corresponding Author

* Chunyu Zhu - School of Low-carbon Energy and Power Engineering, China University of Mining and Technology, Xuzhou 221116, China

* Ruijie Zhu - Graduate School of Chemical Sciences and Engineering, Hokkaido University, Sapporo, Hokkaido 060-8628, Japan

E-mail: zcyls@cumt.edu.cn

vjb92682@elms.hokudai.ac.jp

Keywords

aqueous zinc-ion battereies, freeze drying, hierarchical structure, manganese dioxide, current collector.

Supplemental Experiments

Preparation of the carbon cloth: The cotton cloth was boiled in 1 wt% NaOH for 1 h, and was washed by DI-water for several times. Then, the cotton cloth was pyrolyzed in a tube furnace at 1500 ℃ for 2h, the protective gas was argon (Ar).

Preparation of MnO_2 cathodes: The preparation of α-MnO_2 nanowire is consistent with our previous reports. [25] Briefly, $MnSO_4$ and $KMnO_4$ were dissolved in DI water with a molar ratio of 5:2, and The MnO_2 nanowire was obtained through a 12 h hydrothermal reaction under 140 ℃.

To prepare the HPCF@MnO_2 cathode, first, MnO_2, Ketjen Black (KB), and carboxymethyl cellulose (CMC, MACKLIN) with a weight ratio of 7:2:1, were mixed in DI-water to form a slurry. Then the slurry was added onto the carbon cloth, and the obtained composite material was kept in a vacuum box for 20 min at room temperature. The freeze-drying process was processed after taking out the vacuum treated sample, and the whole freeze-drying process took 24h at -70 ℃. PVDF was dissolved in dimethylformamide (DMF) to form a 0.1 wt% solution and 500 μL was added dropwise to the freeze-dried material, the HPCF@MnO_2 cathode can be obtained after vacuum drying for 36h at room temperature. The MnO_2 loading on the HPCF@MnO_2 cathode was about 1.8 mg cm^{-2}.

To prepare the OCF@MnO_2 cathode, MnO_2, KB, and PVDF were mixed in DI-water with a weight ratio of 7:2:1 to form a slurry. The slurry was then added onto the carbon cloth, after vacuum drying at room temperature for 36 h, the OCF@MnO_2 cathode can be obtained. The MnO_2 loading on the OCF@MnO_2 cathode was about 1.8 mg cm^{-2}.

To prepare the Ti mesh@MnO_2 cathode, MnO_2, KB, and PTFE were mixed in DI-water with a weight ratio of 7:2:1 to form a slurry. The Ti mesh@MnO_2 cathode was prepared by pressing the slurry onto a titanium mesh (100 mesh), and a vacuum drying process was conducted for 36 h under room temperature. The MnO_2 loading on the Ti mesh@MnO_2 cathode was about 1.8 mg cm^{-2}.

Electrochemical tests: Zn||MnO_2 coin cells were assembled by using Zn metal foil as anode and the prepared MnO_2 electrode as cathode. Both the anode and cathode were cut into disk with a diameter of 12 mm, 2 mol L^{-1} $ZnSO_4$ with 0.2 mol L^{-1} $MnSO_4$ was used as electrolyte and a piece of glass-fiber was used as the separator. The electrolyte added to each cell was 200 μL. The cycling tests were conducted on a multi-channel battery tester (LANHE CT3001A). The cut-off voltages for the Zn||MnO_2 cells were 0.8 V (for discharging) and 1.85 V (for charging). The charging/discharging rates tested were 0.5 C, 1 C, 3 C, 5 C and 10 C (1 C = 308 mA g^{-1}). The EIS and CV tests were measured by using an electrochemical workstation (CHENHUA CHI760E). The frequency range of

the EIS tests was 10000Hz-0.1Hz, and the sweep rates for the CV tests were 0.1, 0.15, 0.2, 0.25, 0.3, and 0.35 mV s^{-1}.

GITT tests for Zn || MnO_2 cell: The GITT test for Zn || MnO_2 cells was conducted by intermittently discharging the cell until the cell voltage reached the cut-off voltage. Here, the Zn || MnO_2 cell was firstly charged at 1 C until the cell voltage reached 1.85 V. To finish the GITT test, the cell was discharged at 1 C for 60 s and would rest for 120 min for the completion of ion-diffusion, which was called one cycle. The cycle would be processed until the voltage achieved the cut-off voltage of 0.8 V, then the GITT test would be stopped.

Simulation: Multi-physics simulation details: Electrochemical models were built by using COMSOL Multiphysics with the "2D-Tertiary Current Distribution-Nernst-Planck" interface, which is commonly used in the system with a significant concentration gradient, to describe the current and potential distribution in an electrochemical cell. Here, Nernst-Planck equation can be written as the following form:

$$\frac{\partial c_i}{\partial t} = -\frac{\partial J_i}{\partial x} = \frac{\partial}{\partial x}[D_i \frac{\partial c_i}{\partial x} + D_i c_i (\frac{z_i F}{RT} \frac{\partial \phi}{\partial x})] \quad \textbf{(Eq. S1)}$$

Where c_i is the concentration of the depicted carrier (anion or cation), t is the time, J_i is the mass flux of the depicted carrier, ∂_x refers to the displacement of the depicted species, D_i is the diffusion coefficient of the depicted carrier, z_i is the charge of the depicted carrier,

Φ is the electrostatic potential, while R, F, T are the ideal gas constant, Faraday's constant and temperature (thermodynamic temperature scale), respectively. The Nernst-Planck equation depicted the concentration c_i under equilibrium in one-dimension. A pre-defined Butler-Volmer equation was used to express the electrode reaction under dynamic condition. Here the charge/discharge reaction of MnO_2 is assumed to be a simple insertion/de-insertion reaction between ions and MnO_2.

Simulation of the capacitive current: The current that were contributed by pseudocapacitance and the double-layer capacitance were evaluated by:

$$I = av^b \qquad \textbf{(Eq. S2)}$$

Where i is the current and v is the sweep rate, a is an adjustable parameter, b is the slope of the plot of log i vs log v. Eq. S2 can be modified to the following form in a separated CV cycle:

$$I(V)/v^{0.5} = k_1v^{0.5}+k_2 \qquad \textbf{(Eq. S3)}$$

where $I(V)$ is the measured current at a specific voltage during a single CV cycle, k_1 and k_2 are two parameters that can be obtained by linear fitting every $I(V)/v^{0.5}$ and $v^{0.5}$. The product of k_1 and v (the result is current) is regarded as the contribution from pseudo-capacity. By drawing a plot of k_1v and V, figure of the capacitive current can be obtained.

Characterization: X-ray diffraction (XRD) patterns were collected on an X-ray diffractometer (Rigaku MiniFlex600) by using Cu Ka radiation. Scanning electron microscopy (SEM) observations and energy dispersive spectroscopy (EDS) measurements were conducted on a ZEISS Sigma 500 SEM system. The specific surface areas (SSA) and pore-size distribution were evaluated by nitrogen adsorption method using a surface analyzer, Belsorp-mini (Microtrac). The SSA was calculated by the Brunauer−Emmett−Teller (BET) method, and the pore-size distributions was evaluated by Barrett−Joyner−Halenda (BJH) method and non-local density functional theory (NLDFT) method. The evaluation of pore-size distribution is based on the adsorption process, and the calculation model that comes with the BELMaster software was employed directly. Atomic force microscopy (AFM) tests were conducted on an AFM (Hitachi, NanonaviSII). The 3D morphology reconstruction and micron-sized pore distribution analysis were conducted on a laser scanning confocal microscope (LSCM, Lasertec Co. 1LM21D). The SAXS results were collected on a SAXS equipment (Rigaku Nano-viewer IP). The XPS depth profile were obtained by X-ray photoelectron spectroscopy (XPS, JEOL, JPS-9200) system using Mg-Kα X-ray source.

Supplemental Figures

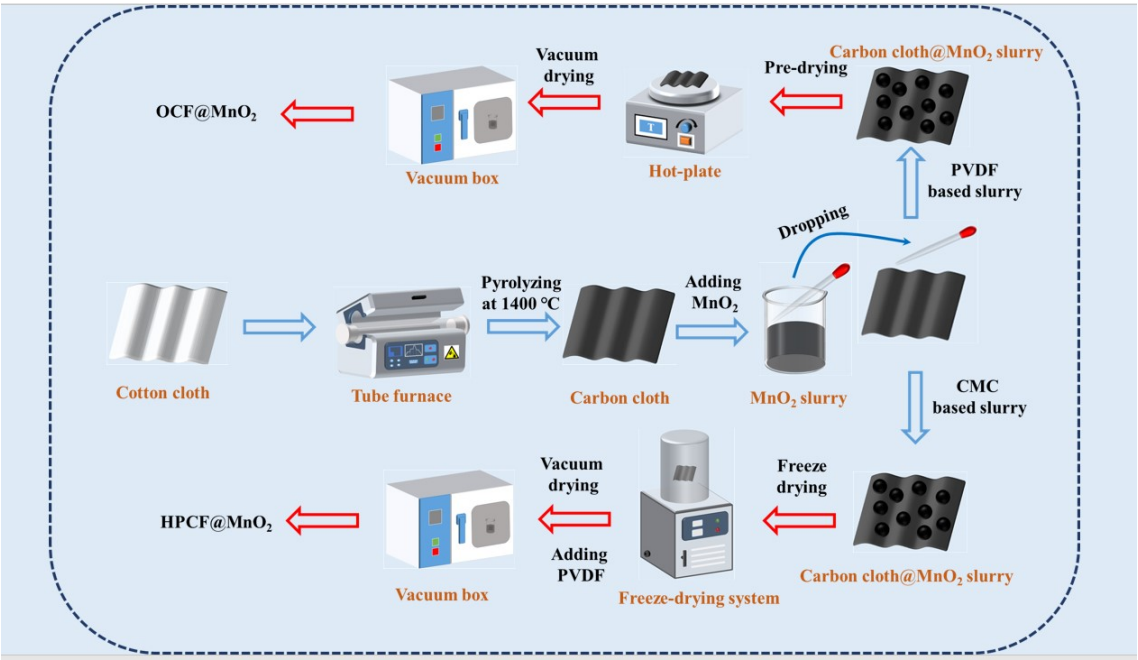

Figure S1 Schematic illustration for the preparation of different samples.

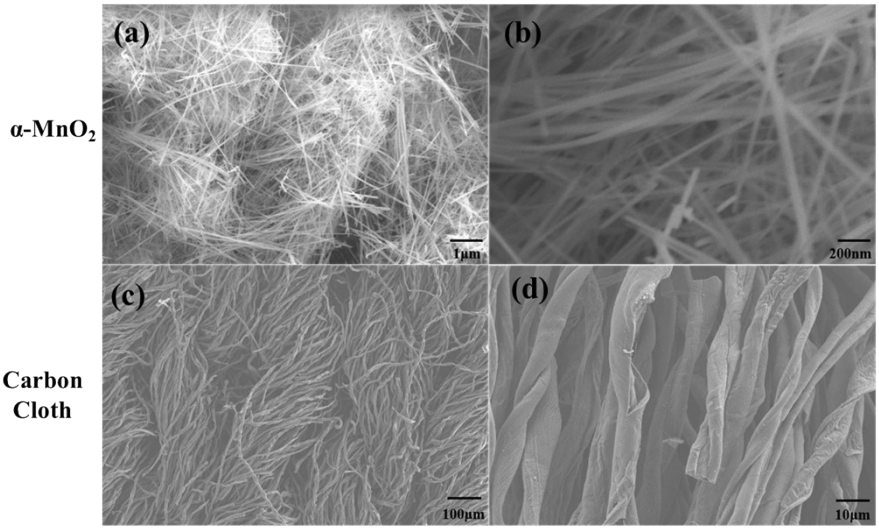

Figure S2 SEM images of (a)(b) α-MnO_2 nanowire and (c)(d) carbon cloth.

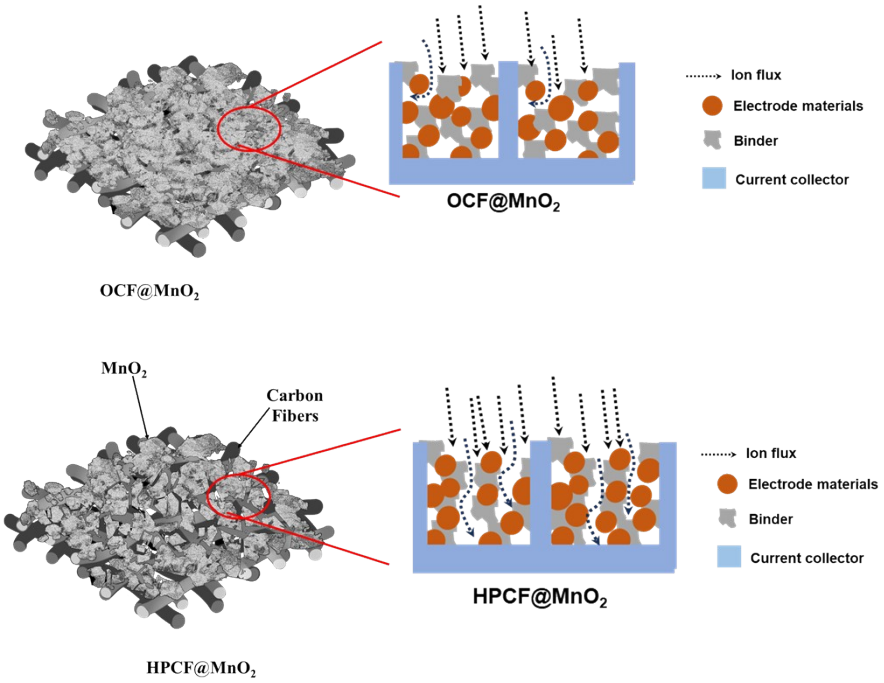

Figure S3 Schematic illustration of different samples.

The reasons for choosing these three electrodes include: 1. The use of Ti mesh and PTFE is currently the most mainstream method of making MnO_2 cathodes for RAZIBs, but PTFE suffers from the problems of poor adhesion and high hydrophobicity that we have mentioned. 2. PVDF is the more commonly used binder in battery industry, with good adhesion and stability, which is suitable for a variety of electrode preparation methods, but PVDF is also hydrophobic, and when applied to the aqueous batteries, it will greatly affect the battery performance, especially under high current density. In this experiment, we consider a simple and scalable way to reduce the negative effect of using PVDF by designing electrode architectures.

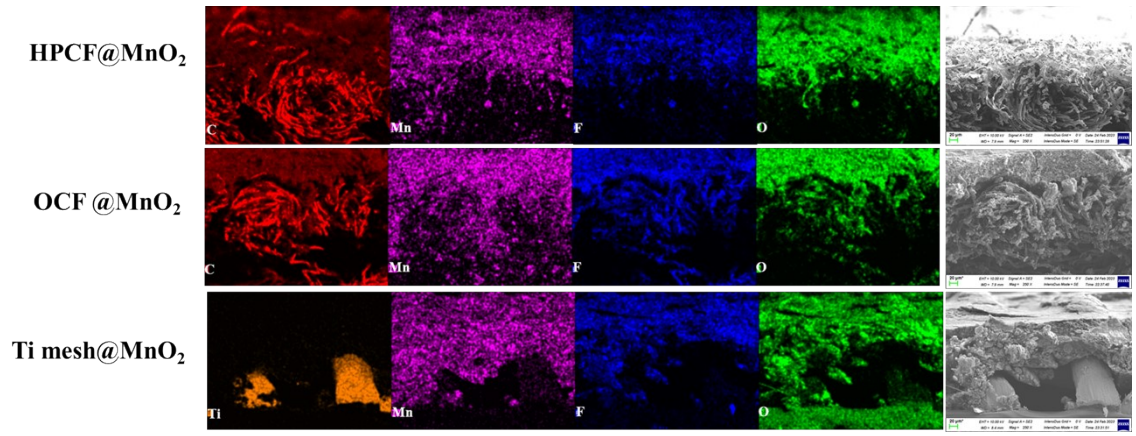

Figure S4 EDS mapping of different samples before cycling.

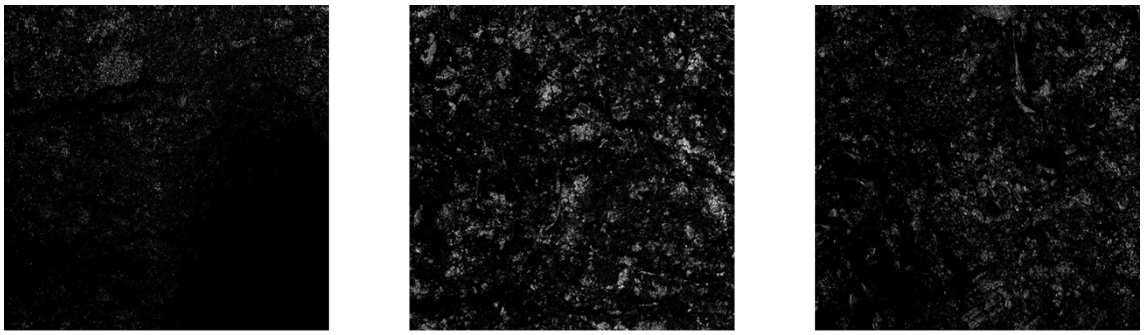

Figure S5 2D images of the LSCM for different samples

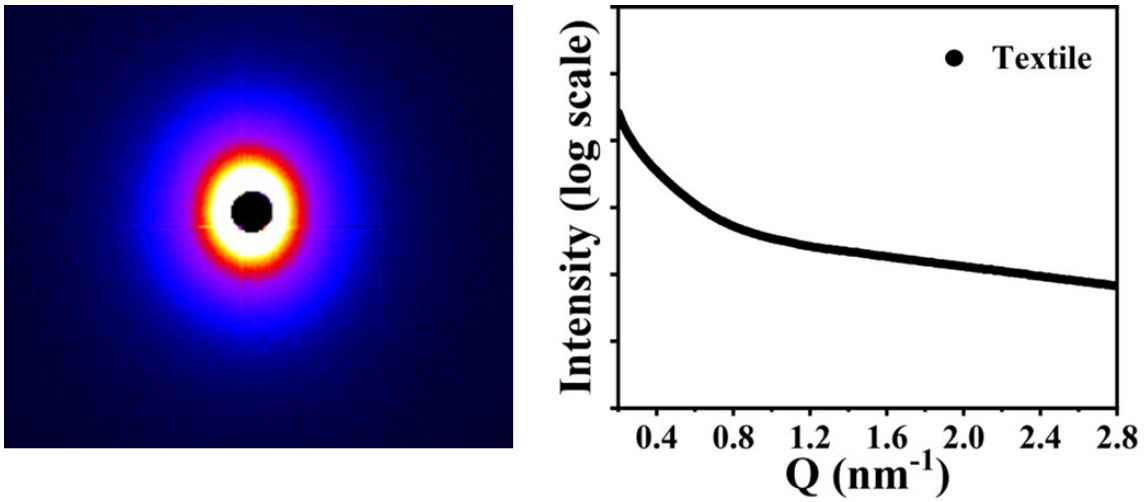

Figure S6 2D SAXS pattern of the carbon cloth (left) and the SAXS results of the carbon cloth (right).

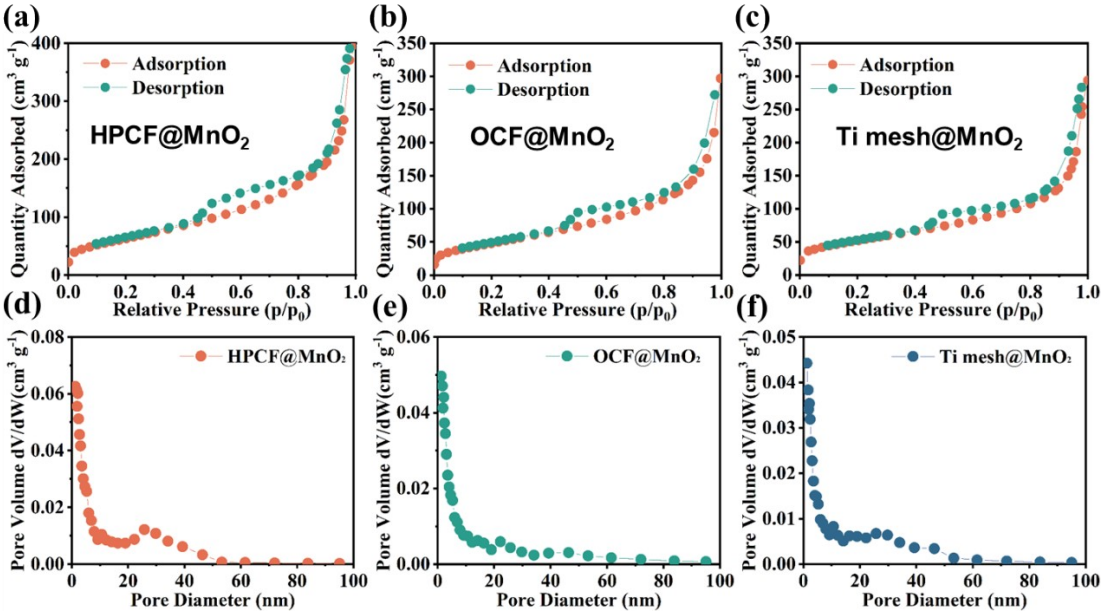

Figure S7 Nitrogen adsorption/desorption curves of (a) HPCF@MnO_2, (b) OCF@MnO_2, and (c) Ti mesh@MnO_2. BJH pore-size distribution analysis of (d) HPCF@MnO_2, (e) OCF@MnO_2, and (f) Ti mesh@MnO_2.

For the preparation of BET samples, all three samples were tested by carefully peeling the materials off the substrates (carbon cloth or Ti mesh), namely, only the portion that did not contain the substrate was tested.

The BET SSA of HPCF@MnO_2, OCF@MnO_2, and Ti mesh@MnO_2 are 220 $m^2\ g^{-1}$, 182 $m^2\ g^{-1}$, and 166 $m^2\ g^{-1}$, respectively.

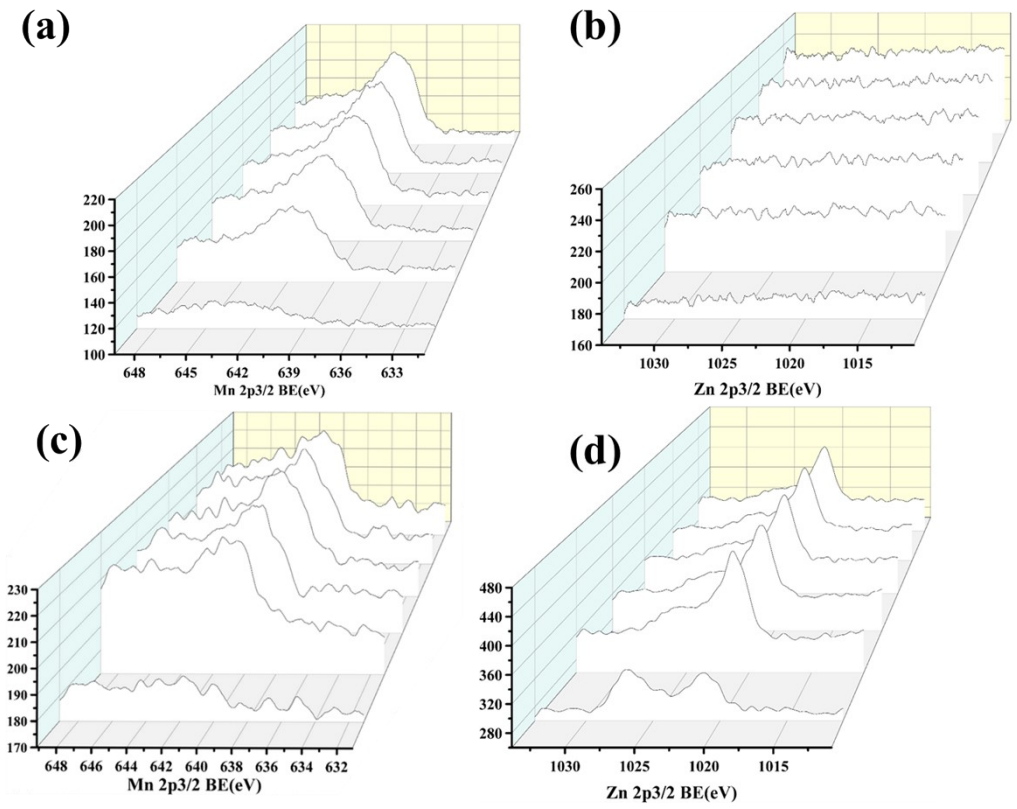

Figure S8 XPS depth profiles for HPCF@MnO_2 before and after one cycle. XPS results of (a) Mn 2p spectra and (b) Zn 2p spectra from HPCF@MnO_2 before one cycle. XPS results of (c) Mn 2p spectra and (d) Zn 2p spectra from HPCF@MnO_2 after one cycle

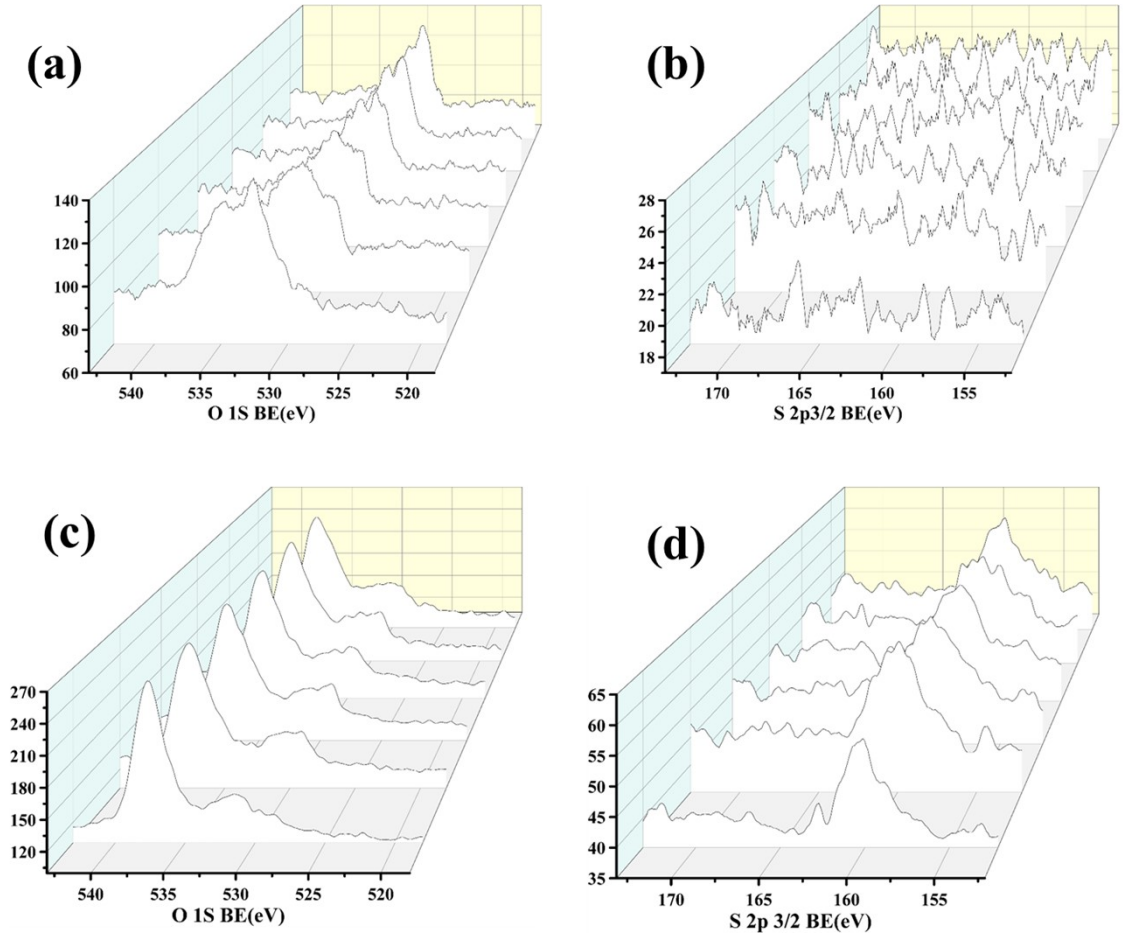

Figure S9 XPS depth profiles for HPCF@MnO_2 before and after one cycle. XPS results of (a) O 1s spectra and (b) S 2p spectra from HPCF@MnO_2 before one cycle. XPS results of (c) O 1s spectra and (d) S 2p spectra from HPCF@MnO_2 after one cycle.

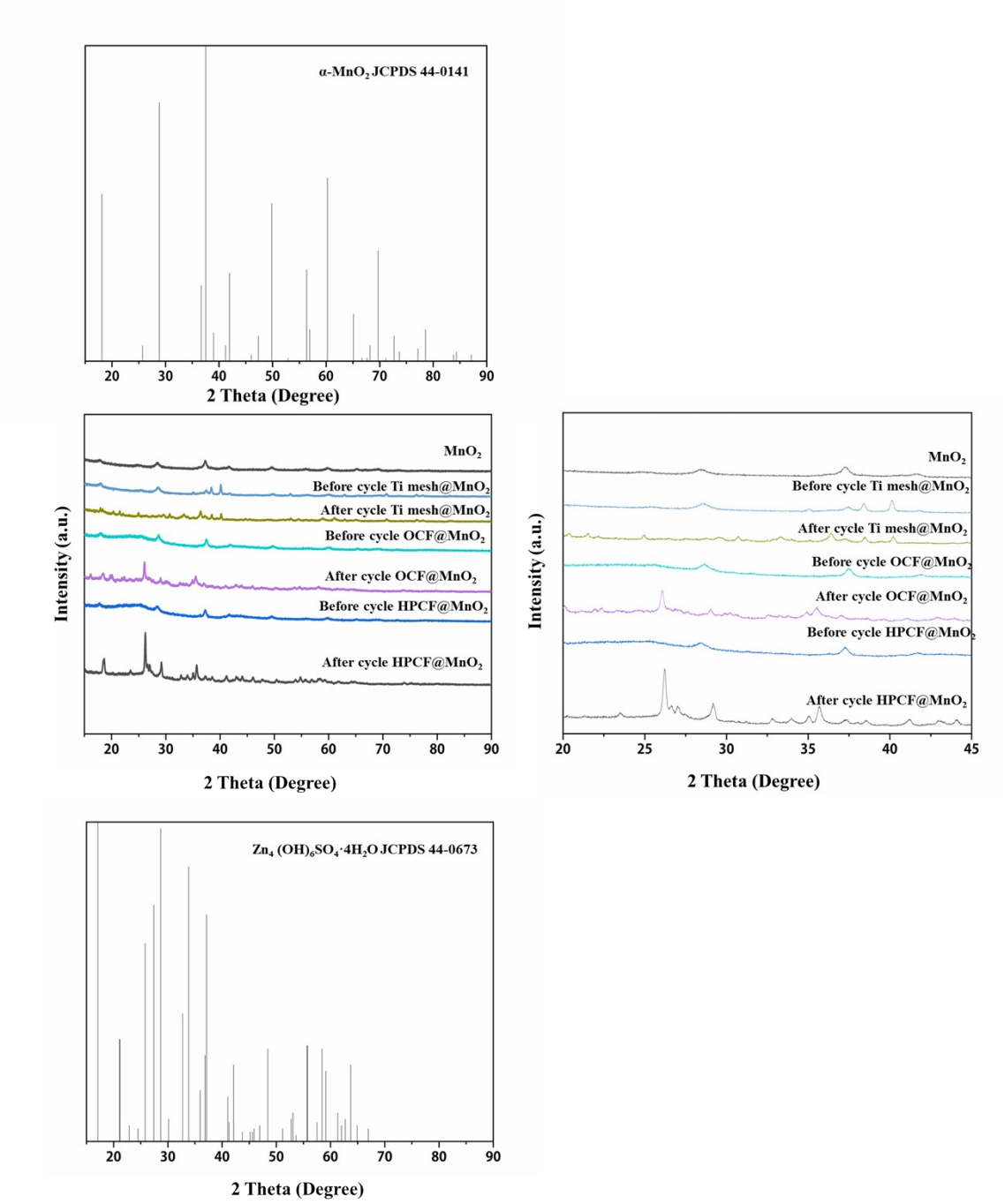

Figure S10 XRD of different samples before and after cycling.

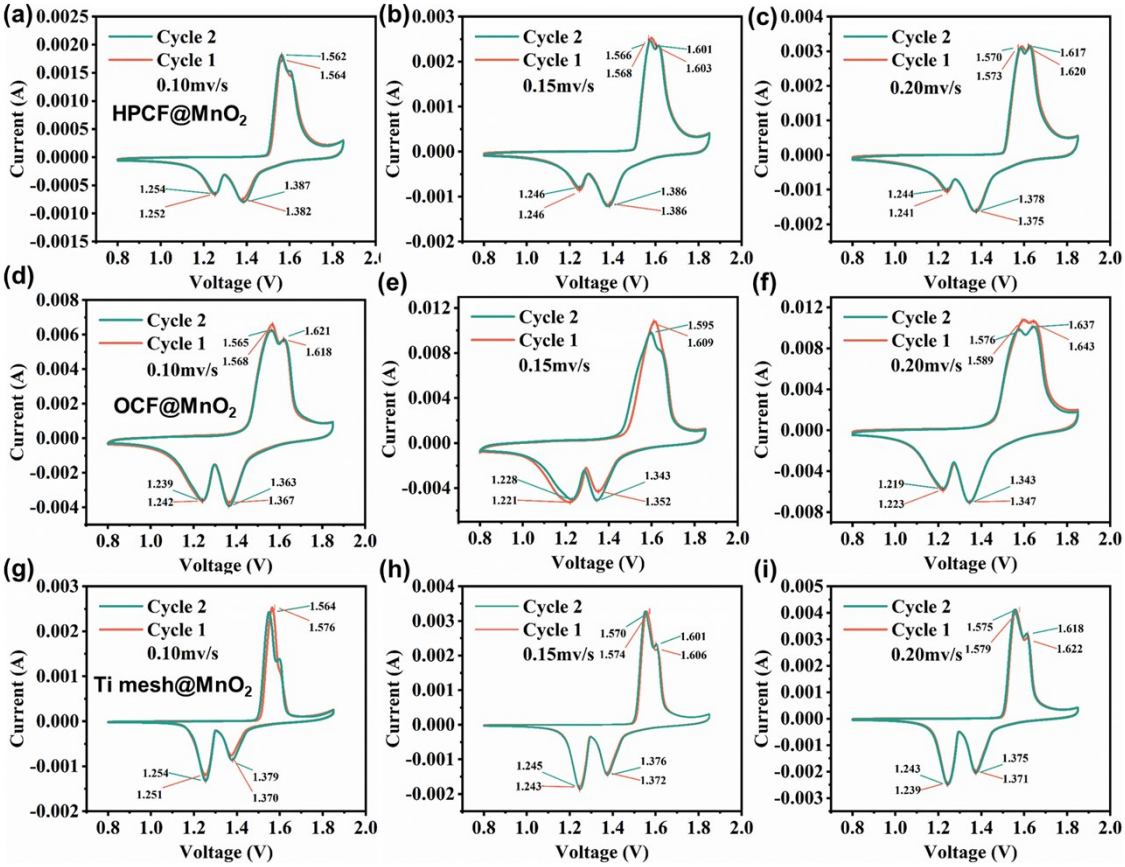

Figure S11 CV curves of different samples under different sweep rates. (a) HPCF@MnO_2 tested under mV s^{-1}, (b) HPCF@MnO_2 tested under mV s^{-1}, (c) HPCF@MnO_2 tested under mV s^{-1}, (d) OCF@MnO_2 tested under mV s^{-1}, (e)OCF@MnO_2 tested under mV s^{-1}, (f) OCF@MnO_2 tested under mV s^{-1}, (g) Ti mesh@MnO_2 tested under mV s^{-1}, (h) Ti mesh@MnO_2 tested under mV s^{-1}, (i) Ti mesh@MnO_2 tested under mV s^{-1}.

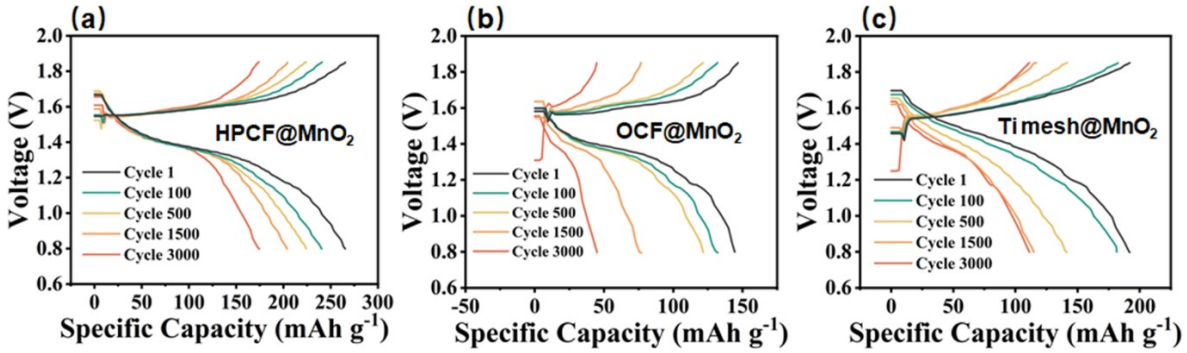

Figure S12 Voltage profiles of different samples at different cycles. (a) HPCF@MnO_2, (b)OCF@MnO_2, and (c) Ti mesh@MnO_2.

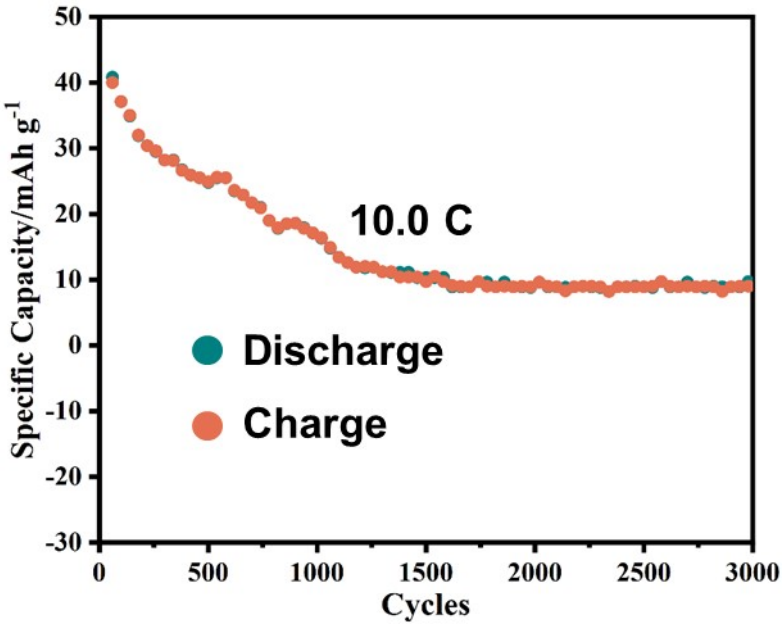

Figure S13 Specific capacity provided by the conductive carbon (1C = 308 mA g^{-1}).

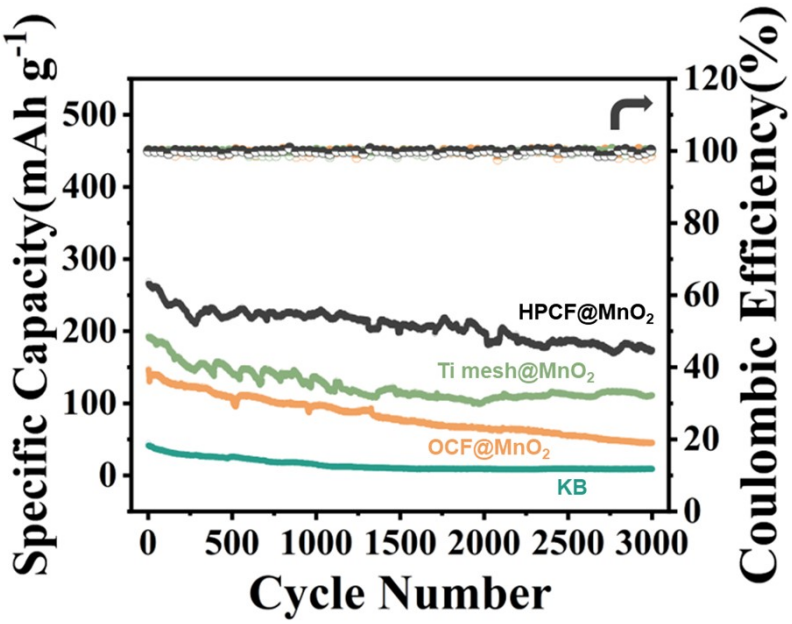

Figure S14 A comparison in the cycling performance of different samples.

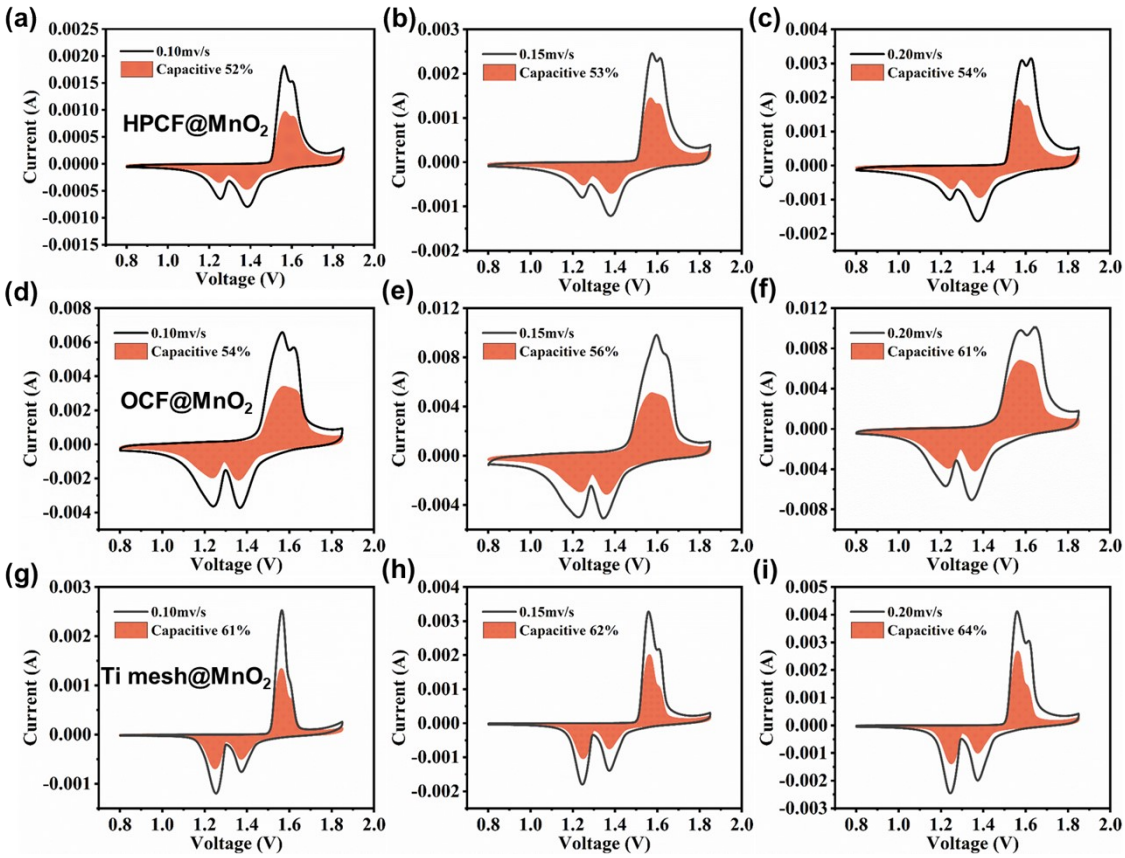

Figure S15 Simulated capacitive current of (a) HPCF@MnO_2 tested under 0.1 mV s^{-1}, (b) HPCF@MnO_2 tested under 0.15 mV s^{-1}, (c) HPCF@MnO_2 tested under 0.2 mV s^{-1}, (d) OCF@MnO_2 tested under 0.1 mV s^{-1}, (e) OCF@MnO_2 tested under 0.15 mV s^{-1}, (f) OCF@MnO_2 tested under 0.2 mV s^{-1}, (g) Ti mesh@MnO_2 tested under 0.1 mV s^{-1}, (h) Ti mesh@MnO_2 tested under 0.15 mV s^{-1}, (i) Ti mesh@MnO_2 tested under 0.2 mV s^{-1}.

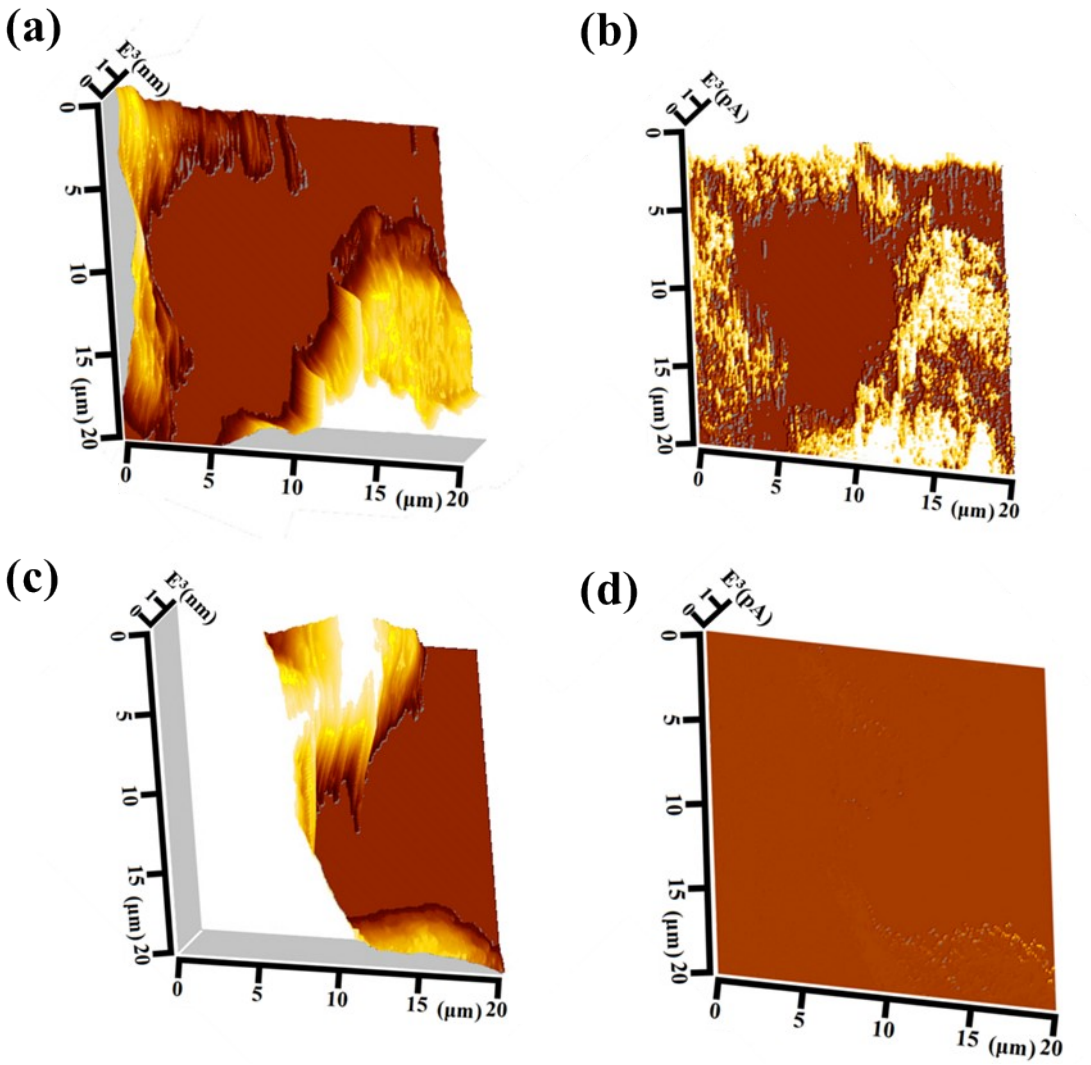

Figure S16 c-AFM measurements of different samples. Morphology images of (a) HPCF@MnO_2 and (c) Ti mesh@MnO_2. Current images of (b) HPCF@MnO_2 and (d) Ti mesh@MnO_2.

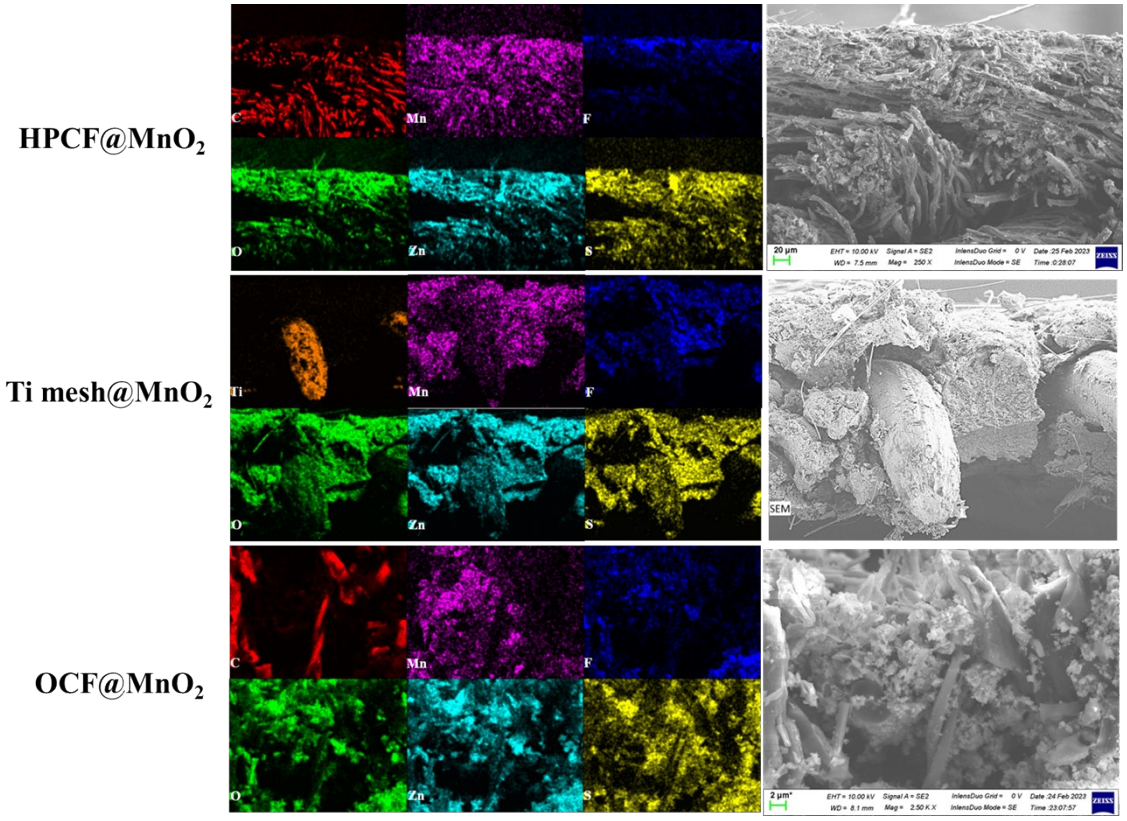

Figure S17 EDS mapping of different samples after cycling.

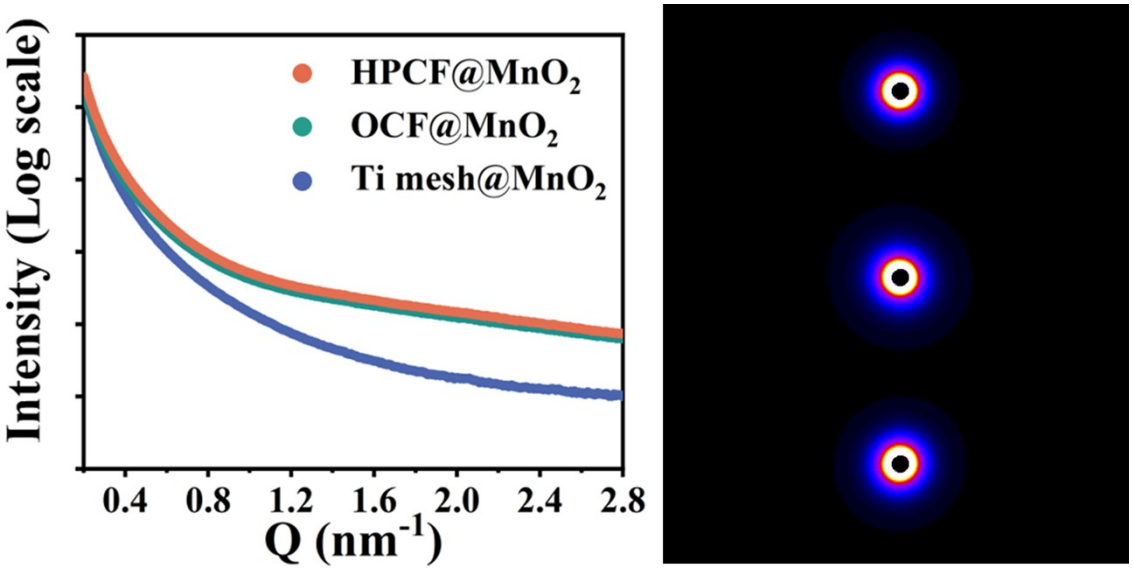

Figure S18 SAXS results of different samples after cycling.

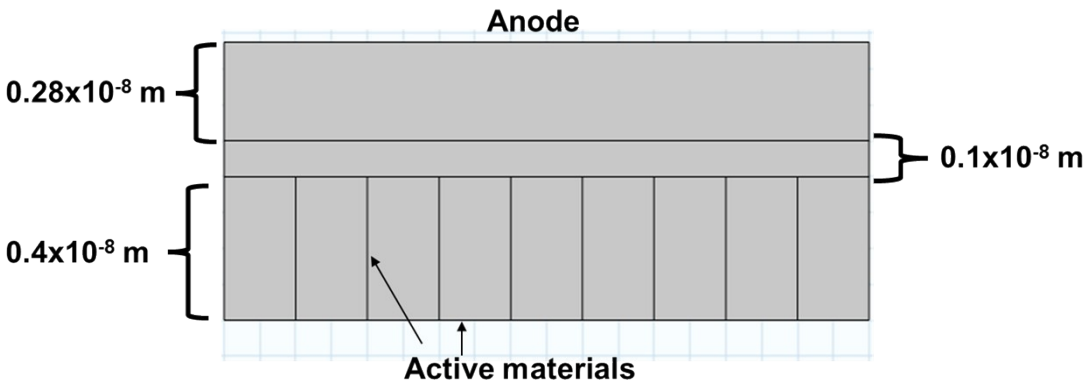

Figure S19 The geometry of the simulation model.

Table S1 Capacity retention of different cells tested under different charging/discharging rates.

Materials	Specific Capacity (mAh g^{-1})									
	0.5 C	**1.0 C**	**%**	**3.0 C**	**%**	**5.0 C**	**%**	**10.0 C**	**%**	**0.5-10.0 C(%)**
HPCF@MnO_2	518	426	82	366	86	325	89	265	82	**51**
OCF@MnO_2	340	319	94	232	73	190	82	138	73	**40**
Ti mesh@MnO_2	333	290	87	240	83	221	92	167	87	**50**

Table S2 Comparison of different optimization strategies for MnO_2 cathodes.

Materials	Zn || MnO_2				Ref
	m(MnO_2)	**(Dis)charge rate**	**Cycles**	**Specific Capacity**	
PCNT@MnO_2	-	1000 mA g^{-1}	300	104.9 mAh g^{-1}	1
NCM@MnO_2	-	1000 mA g^{-1}	1000	192.0 mAh g^{-1}	2
PDA-y@MnO_2	1.0 mg cm^{-2}	1000 mA g^{-1}	3500	200.0 mAh g^{-1}	3
HNNM@MnO_2	0.2 mg cm^{-2}	1500 mA g^{-1}	500	150.0 mAh g^{-1}	4
CNTs-3@MnO_2	--	2000 mA g^{-1}	2000	116.0 mAh g^{-1}	5
KMO/CNFs@MnO_2	-	3000 mA g^{-1}	1000	190.0 mAh g^{-1}	6
Biochar@ MnO_2	-	3000 mA g^{-1}	1000	212.8 mAh g^{-1}	7

MOC-5@MnO_2	1.5 mg cm^{-2}	3000 mA g^{-1}	2750	130.0 mAh g^{-1}	8
CNT@MnO_2	-	3000 mA g^{-1}	5000	95.6 mAh g^{-1}	9
HPCF@MnO_2	1.8 mg cm^{-2}	3000 mA g^{-1}	3000	180.2 mAh g^{-1}	This study

Reference

1. H. Peng, F. Q. Wang, D. Y. Wang, S. Z. Cui, W. B. Hou and G. F. Ma, *ACS Applied Energy Materials*, 2022, 5, 3854-3862.

2. S. Luo, J. Xu, B. Yuan, L. Xu, R. Zheng, Y. Wang, M. Zhang, Y. Lu and Y. Luo, *Carbon*, 2023, 203, 326-336.

3. B. Wang, Y. Zeng, P. Chen, J. Hu, P. Gao, J. T. Xu, K. K. Guo and J. L. Liu, *ACS Appl Mater Interfaces*, 2022, 14, 36079-36091.

4. S. Y. Su, Y. Xu, Y. Wang, X. Y. Wang, L. Shi, D. Wu, P. C. Zou, A. Nairan, Z. Y. Lin, F. Y. Kang and C. Yang, *Chemical Engineering Journal*, 2019, 370, 330-336.

5. J. Xie, G. Liu, J. Sun, R. Zheng, W. Zhao, T. Chu, H. Lin, Y. Xu, S. Gao and Z. Sui, *Diamond and Related Materials*, 2022, 125.

6. J. Yang, G. Yao, Z. Q. Li, Y. H. Zhang, L. Z. Wei, H. L. Niu, Q. W. Chen and F. C. Zheng, *Small*, 2023, 19.

7. H. B. He, Z. Liu, Z. X. Luo, Z. H. Zhang, Y. Chen and J. Zeng, *Journal of Alloys and Compounds*, 2023, 960.

8. X. J. Chen, W. Li, Z. P. Zeng, D. Reed, X. L. Li and X. B. Liu, *Chemical Engineering Journal*, 2021, 405.

9. D. D. Jia, Z. W. Yang, W. Gu and X. Liu, *Journal of Alloys and Compounds*,

2022, 910.